Shape-Controlled Colloidal Interactions in Nematic Liquid Crystals

Clayton P. Lapointe,[1,2] Thomas G. Mason,[2] Ivan I. Smalyukh[1]*

Robust control over the positions, orientations, and assembly of nonspherical colloids may aid in the creation of new types of structured composite materials that are important from both technological and fundamental standpoints. With the use of lithographically fabricated equilateral polygonal platelets, we demonstrate that colloidal interactions and self-assembly in anisotropic nematic fluids can be effectively tailored via control over the particles' shapes. The particles disturb the uniform alignment of the surrounding nematic host, resulting in both a distinct equilibrium alignment and highly directional pair interactions. Interparticle forces between polygonal platelets exhibit either dipolar or quadrupolar symmetries, depending on whether their number of sides is odd or even, and drive the assembly of a number of ensuing self-assembled colloidal structures.

Self-assembly of micrometer- and nanometer-scale colloidal particles into ordered structures is of wide-ranging interest for both fundamental science and technological applications (*1*). In isotropic liquids such as water, the electrostatic and entropic forces that drive the assembly of spherical colloids are typically isotropic, limiting the overall landscape of possible structures. Concentrated suspensions of monodisperse spherical particles are an important example; these can form three-dimensional (3D) colloidal crystals that are markedly similar to their atomic counterparts. However, colloidal crystals formed in this fashion are restricted to lattices with high packing fractions, such as hexagonal close-packed or face-centered cubic (*2*). The generation of anisotropic interactions is necessary to increase the complexity and diversity of colloidal architectures formed by such interactions (*3*–*6*). Oriented assemblies of particles can be produced by means such as nonuniform patterning of their surfaces (*3*), anisotropic deposition of colloids onto solid substrates (*4*), or application of external fields (*5*). Alternatively, introducing anisotropy directly into a solvent by using a nematic liquid crystal (NLC), one can engender anisotropic interaction forces between colloids that are not present in ordinary fluids (*7*). NLCs are composed of rod-shaped molecules with long molecular axes aligned along a common direction (*8*). The local average molecular orientation is often represented by a unit vector $\mathbf{n}$ with inversion symmetry $\mathbf{n} \equiv -\mathbf{n}$, referred to as the director. The dependence of $\mathbf{n}$ as a function of spatial position $\mathbf{r}$ is described with a director field $\mathbf{n}(\mathbf{r})$. Anisotropic molecular interactions at NLC surfaces, known as surface anchoring, result in a preferential alignment and boundary conditions for $\mathbf{n}(\mathbf{r})$. Colloids immersed in NLCs deform the surrounding director field because of this surface anchoring and induce point or line defects [regions where $\mathbf{n}(\mathbf{r})$ is discontinuous] in the nematic bulk (Fig. 1, A and B) or at the nematic-particle interface (Fig. 1C), unless the surface anchoring is weak or the particles are small (supporting online material fig. S1) (*9*). The particles and accompanying defects introduce long-range gradients in $\mathbf{n}(\mathbf{r})$ that depend on particle size (*9*), type and strength of surface anchoring (*10*), confinement (*11*, *12*), and external fields (*13*). The elastic energy due to these gradients depends on the particles' relative positions and gives rise to interactions mediated by elasticity. Even for spherical particles in NLCs (Fig. 1, A to C), elastic interactions are highly anisotropic and can lead to a host of self-assembled structures ranging from linear and branched chains to 2D crystals (*7*, *9*–*16*). Reminiscent of electrostatic interactions exhibited by charge distributions, elastic colloidal interactions bear qualitatively different symmetries that mimic the dipolar (Fig. 1A) or quadrupolar (Fig. 1, B and C) symmetries of $\mathbf{n}(\mathbf{r})$ around isolated particles.

We demonstrate that altering the shapes of particles can lead to marked changes in the symmetry of their elastic interactions and the resulting colloidal assemblies in NLCs. Optical polarizing microscopy (PM) and fluorescence confocal polarizing microscopy (FCPM) show

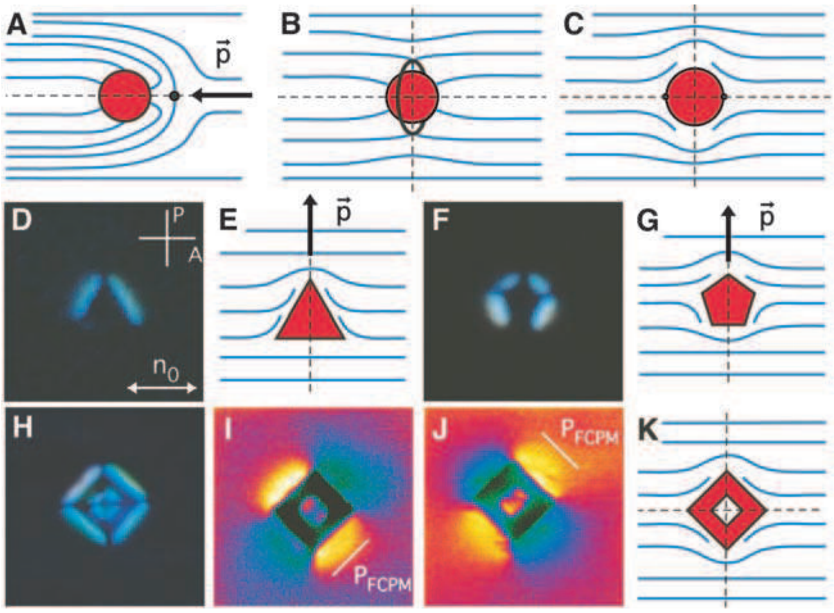

Fig. 1. Shape-controlled director field configurations around colloidal particles immersed in a uniformly aligned NLC. (**A**) A spherical colloid with strong vertical anchoring induces a hyperbolic point defect (black dot) in the bulk of the NLC forming a dipolar $\mathbf{n}(\mathbf{r})$ structure (blue lines) with the elastic dipole moment $\mathbf{p}$ parallel to $\mathbf{n}_0$. (**B**) A spherical particle with vertical anchoring and encircled by a line defect in the equatorial plane (black line) gives a quadrupolar director structure. (**C**) A colloidal sphere with planar degenerate anchoring induces two surface point defects (black dots) at the poles along $\mathbf{n}_0$ and forms a quadrupolar configuration of $\mathbf{n}(\mathbf{r})$. Optical PM micrographs show that polygons with an odd number of sides, such as triangles (**D** and **E**) and pentagons (**F** and **G**), in 5CB orient with one side parallel to $\mathbf{n}_0$ and, as shown in (E and G), induce dipolar $\mathbf{n}(\mathbf{r})$ with elastic dipole moments $\mathbf{p}$ perpendicular to $\mathbf{n}_0$. (**H**) PM image showing a square platelet oriented with its diagonal axis parallel to $\mathbf{n}_0$ producing quadrupolar distortions. (**I** and **J**) FCPM images of $\mathbf{n}(\mathbf{r})$ obtained for linear polarizations (P_{FCPM}) at ±45° to $\mathbf{n}_0$, and color-coded fluorescence intensity varying from minimum (black) to increasingly higher intermediate (green, blue, red) and maximum (yellow) values. (**K**) Reconstructed quadrupolar director field for a square platelet in 5CB. Dashed lines denote mirror symmetry planes of the $\mathbf{n}(\mathbf{r})$ configurations. The lateral edge lengths of triangles, squares, and pentagons are 3.0 μm, 4.5 μm, and 1.5 μm, respectively. All platelets have a thickness of 1 μm. The square-shaped particles contain a square hole with 2-μm sides.

---

[1] Department of Physics, Renewable and Sustainable Energy Institute, and Liquid Crystals Materials Research Center, University of Colorado at Boulder, Boulder, CO 80309, USA. [2] Department of Chemistry and Biochemistry, Department of Physics and Astronomy, and California NanoSystems Institute, University of California at Los Angeles, Los Angeles, CA 90095, USA.

*To whom correspondence should be addressed. E-mail: ivan.smalyukh@colorado.edu

that platelet colloids with equilateral polygonal shapes exhibit well-defined alignment and elastic deformations of $\mathbf{n}(\mathbf{r})$ that have either dipolar or quadrupolar symmetry. Colloidal polygons with an odd number of sides form elastic dipoles, whereas even-sided particles form elastic quadrupoles. Using model polygonal platelets shaped as triangles, squares, and pentagons, we demonstrate that their shape dictates the resulting $\mathbf{n}(\mathbf{r})$ symmetry as well as the symmetry of the ensuing elastic interactions. Particle tracking video microscopy (*17*), combined with optical tweezing of particle pairs, provides direct measurements of anisotropic interaction forces.

Monodisperse platelet colloids of uniform thickness and predesigned shapes are fabricated with the use of photolithography (*18*). Micron-sized polygonal colloids of triangular, square, and pentagonal shapes are produced using an ultraviolet-sensitive photoresist (SU-8) on Si wafers (*19*). After exposure and development, the particles are released from the wafers into an organic solvent and transferred into pentylcyanobiphenyl (5CB), a room temperature NLC. Sample cells consisting of parallel glass plates separated by 10- to 60-μm spacers are filled with colloidal dispersions in 5CB by capillary action and sealed with epoxy. The far-field alignment direction $\mathbf{n}_0$ is set by unidirectional rubbing of the polyimide coated inner surfaces of the cell. The samples are studied with an inverted optical microscope equipped with a confocal laser scanning unit and a holographic optical tweezers system (*20*) operating at $\lambda = 1064$ nm. The 3D structure of $\mathbf{n}(\mathbf{r})$ around the colloids is determined with lateral and vertical resolution of ~0.5 μm with the use of FCPM (*21*). For FCPM observations, 0.01 weight percent of anisotropic fluorescent dye was dissolved homogeneously in 5CB (*19*); at this concentration, the rodlike dye molecules do not alter the NLC properties and orient parallel to 5CB molecules so that the contrast in the fluorescence image arises from spatial changes in $\mathbf{n}(\mathbf{r})$ (*21*). Imaging and optical tweezing are performed simultaneously with a 100× oil-immersion objective.

PM images reveal the $\mathbf{n}(\mathbf{r})$ deformations surrounding isolated particles of each type suspended in aligned 5CB (Fig. 1). When $\mathbf{n}_0$ is oriented along the linear polarization of incident light, distorted regions where $\mathbf{n}(\mathbf{r})$ departs from $\mathbf{n}_0$ alter the polarization state of transmitted light and appear bright when viewed through the analyzer. Polygonal platelets always orient with their larger-area top and bottom surfaces parallel to $\mathbf{n}_0$, suggesting planar degenerate anchoring at the interface of SU-8 and 5CB. Polygons that have an odd number of sides (N), such as triangles and pentagons, orient with one of their sides along $\mathbf{n}_0$, and bright lobes are visible near their other sides (Fig. 1, D and F). However, colloids with even N, such as squares, align with one diagonal axis along $\mathbf{n}_0$, and bright regions appear symmetrically along all outer and inner edges (Fig. 1H). PM and FCPM textures indicate the presence of three mirror symmetry planes of the $\mathbf{n}(\mathbf{r})$ deformations, which intersect the particle's center of mass: one coplanar with both $\mathbf{n}_0$ and the unit vector $\mathbf{v}$ normal to the platelet's larger-area faces, a second parallel to the faces, and a third plane orthogonal to $\mathbf{n}_0$. Thus, the $\mathbf{n}(\mathbf{r})$ structure is quadrupolar, as schematically shown in Fig. 1K, resembling the symmetry of elastic quadrupoles formed by spherical particles (Fig. 1, B and C). Further, because the strongest FCPM signal corresponds to regions where $\mathbf{n}(\mathbf{r})$ is parallel to the linear FCPM polarization, the fluorescence images in Fig. 1, I and J, demonstrate that $\mathbf{n}(\mathbf{r})$ is indeed quadrupolar and consistent with surface anchoring of 5CB on SU-8 photoresist being degenerate planar (*22*).

In the case of triangles and pentagons with odd N, however, the mirror symmetry plane that is coplanar with both $\mathbf{n}_0$ and $\mathbf{v}$ is broken so that the $\mathbf{n}(\mathbf{r})$ structure is dipolar (Fig. 1, E and G), unlike that of other previously studied colloids promoting planar surface anchoring (*15*, *23*). Moreover, the elastic dipole moment $\mathbf{p}$ is orthogonal to $\mathbf{n}_0$ (Fig. 1E), in contrast to what is seen for colloids with vertical surface anchoring and $\mathbf{p}$ parallel to $\mathbf{n}_0$ (*7*, *11*, *14*, *24*), as shown in Fig. 1A. Examples of dipoles that align orthogonally to field lines are rare but can be formed by dipolar pairs of line defects in NLCs (*19*) and vortex spin configurations in ferromagnets (*8*). Similar to a sphere with planar anchoring shown in Fig. 1C, the shape-dictated dipolar structures of odd-N platelets do not give rise to point or line defects in the NLC bulk. The dipolar $\mathbf{n}(\mathbf{r})$ symmetry of odd-N platelets should be stable with respect to varying particle size and the strength of surface anchoring at their interfaces (fig. S1) (*19*). This is different from the case of dipoles formed by spherical colloids accompanied by bulk point defects (Fig. 1A) observed only for strong anchoring and for particle sizes larger than ~1 μm, but not for smaller colloids for which a quadrupolar $\mathbf{n}(\mathbf{r})$ (Fig. 1B) is of lower energy (*9*). For odd-N polygonal platelets, although the magnitude of $\mathbf{p}$ decreases with decreasing particle size or weakening anchoring strength (fig. S1), the alignment and dipolar symmetry should retain down to particle sizes of ~50 to 100 nm, at which the planar boundary conditions at the platelet surfaces are expected to partially relax (*19*). For $N = 5$, the magnitude of $\mathbf{p}$ is smaller than that for $N = 3$ (Fig. 1), and we expect that it decreases further as N increases and ultimately vanishes in the limit $N \to \infty$, corresponding to a circular disc with quadrupolar $\mathbf{n}(\mathbf{r})$ (*9*).

The director field configurations surrounding regular polygons (Fig. 1) can be understood within an elegant theoretical framework that is built on an analogy with electrostatics (*25*–*27*). Within the one–elastic constant approximation (*19*), minimization of the NLC elastic energy $U_{\mathrm{el}} = (K/2)\int d^3\mathbf{r}(\nabla\mathbf{n})^2$ [where K is an average Frank elastic constant, and $(\nabla\mathbf{n})^2 = (\nabla\cdot\mathbf{n})^2 + (\nabla\times\mathbf{n})^2$] leads to Laplace's equation for $\mathbf{n}(\mathbf{r})$. Far from the particle, deviations from $\mathbf{n}_0$ are small, and $\mathbf{n}(\mathbf{r})$ can be expanded in a multipole series containing elastic monopole, dipole, and quadrupole terms that decay with distance r as $1/r$, $1/r^3$, and $1/r^5$, respectively. The predicted absence of an elastic monopole, when no external torque is present (*25*), is consistent with the observed dipolar symmetry of $\mathbf{n}(\mathbf{r})$, as well as the equilibrium orientation of polygons with odd N. For example, $\mathbf{n}(\mathbf{r})$ would have no planes of mirror symmetry for a triangle or pentagon oriented so that all edges are neither parallel nor perpendicular to $\mathbf{n}_0$. Consequently, an elastic torque would be present, and the system would not be in mechanical equilibrium. There are two possible ori-

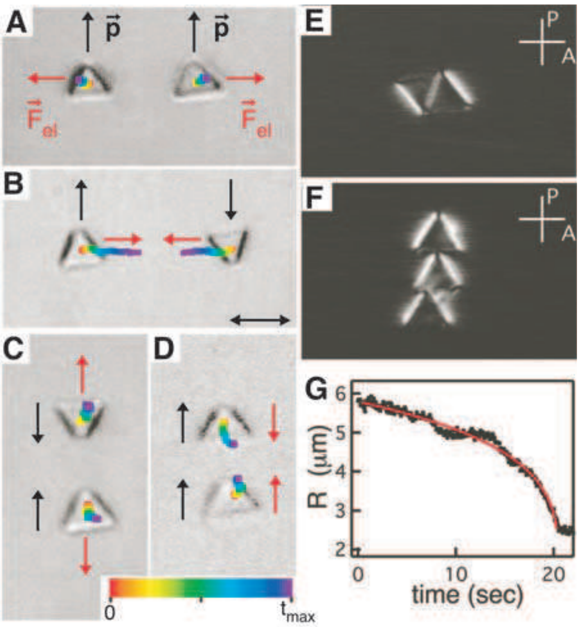

Fig. 2. Elastic dipole-dipole pair interactions of triangular colloids in 5CB and their assembly into chains. (**A** to **D**) Color-coded trajectories of triangles with parallel [(A) and (D)] and antiparallel [(B) and (C)] dipole moments; the trajectories are overlaid on top of the first video frame, with colors representing time according to the scale in the inset. Maximum elapsed times t_{max}: (A) 20.5 s, (B) 29.6 s, (C) 53.3 s, and (D) 24.8 s. Red arrows show the direction of the elastic force $\mathbf{F}_{\mathrm{el}}$. PM images of two types of aggregates: (**E**) antiparallel dipole chain along $\mathbf{n}_0$ and (**F**) parallel dipole chain oriented perpendicular to $\mathbf{n}_0$. (**G**) Time dependence of the pair separation for the trajectories shown in (D). The red curve shows a fit with the expected $R(t)$ for a dipole-dipole attraction balanced by a viscous drag. The direction of the far-field director $\mathbf{n}_0$ is shown by the double-headed arrow in (B).

entations for a triangle or a pentagon with ensuing **n**(**r**) having at least two planes of mirror symmetry: (i) one with a side along $\mathbf{n_0}$ giving an elastic dipole with **p** perpendicular to $\mathbf{n_0}$ and (ii) another with a side oriented perpendicular to $\mathbf{n_0}$ (in this case, **p** would be parallel to $\mathbf{n_0}$). Evidently, the former has lower elastic energy because this is the equilibrium orientation observed in the experiments. The alignment of colloidal polygons with even N, such as square-shaped particles, can be understood in a similar fashion. Orientations for which neither of the diagonals are parallel to $\mathbf{n_0}$ would give rise to an elastic torque and are unstable. When the sample is heated into the isotropic phase, no preferred orientation is observed (fig. S2), confirming the elastic nature of the alignment of polygons in the nematic phase. Furthermore, observations during multiple heating and cooling cycles show that different sides (odd N) and diagonals (even N) can align along $\mathbf{n_0}$ each time the sample is quenched into the nematic phase, demonstrating that there is no preference in the selection of these sides or diagonals.

Although the orientations of the polygonal edges are constrained relative to $\mathbf{n_0}$, a platelet's surface normal **v** is free to rotate about $\mathbf{n_0}$ in the bulk of a ≈60-μm-thick NLC cell, indicating that the elastic energy is independent of such rotations (*28*). Confinement to cells of thickness comparable to the lateral size of platelets (≈10 μm) inhibits rotations about $\mathbf{n_0}$, and the platelike colloids orient parallel to the cell substrates to minimize the elastic energy due to the planar anchoring at the top and bottom surfaces of the colloids. To explore the directionality and strength of anisotropic elastic-pair interactions, we control the initial positions and orientations of particles with the use of optical tweezers (*11*, *12*, *15*) and then track their motion using video microscopy after release from the laser traps. When the center-to-center separation vector **R** for two triangles is along $\mathbf{n_0}$, elastic repulsion occurs for parallel dipoles (Fig. 2A), whereas attraction takes place for antiparallel dipoles (Fig. 2B). The opposite is true for situations when **R** is perpendicular to $\mathbf{n_0}$; antiparallel dipoles repel (Fig. 2C) and parallel dipoles attract (Fig. 2D). Two types of self-assembled chainlike aggregates are observed: (i) antiparallel dipole chains in which the triangles aggregate along $\mathbf{n_0}$ (Fig. 2E) and (ii) chains perpendicular to $\mathbf{n_0}$ consisting of parallel dipoles (Fig. 2F). Chaining of triangular colloids perpendicular to $\mathbf{n_0}$ is a consequence of the dipoles' alignment orthogonal to $\mathbf{n_0}$. The dipolar nature of the elastic interaction is further evidenced by the time dependence of particle separation $R(t)$ for a pair of triangles aggregating along $\mathbf{n_0}$ (Fig. 2G). Because the system is highly overdamped (Reynolds number << 1), inertial forces are negligible and the elastic force F_{el} is balanced by a viscous Stokes drag $F_{\mathrm{drag}} = -\zeta dR/dt$, where ζ is a drag coefficient, and dR/dt is the time-derivative of the particle separation $R(t)$. For an elastic dipolar force $F_{\mathrm{el}} = -\kappa_{\mathrm{d}}/R^4$ (where κ_{d} is a constant that depends on K and the geometry and size of the particle), integration of the equation of motion $F_{\mathrm{el}} + F_{\mathrm{drag}} \approx 0$ yields $R(t) = (R_0^5 - 5\alpha_{\mathrm{d}}t)^{1/5}$, where $\alpha_{\mathrm{d}} = \kappa_{\mathrm{d}}/\zeta$, and R_0 is the initial separation at time $t = 0$ when particles are released from the traps. $R(t)$ fits the data well with one adjustable parameter $\alpha_{\mathrm{d}} = 63.1 \pm 0.5$ μm^5/s (red curve in Fig. 2G). Using an estimate of the drag coefficient $\zeta \sim (2 \text{ to } 4) \times 10^{-6}$ kg/s (*29*) and the maximum relative velocity $dR/dt \approx 1$ μm/s determined from the data in Fig. 2G, one obtains a maximum attractive elastic force of 2 to 4 pN near contact at $R \approx 2.6$ μm. This force and the corresponding binding energy $\approx 5 \times 10^{-18}$ J ($\approx 1200 k_{\mathrm{B}}T$, where k_{B} is Boltzmann's constant) for a pair of triangles are comparable to those measured for spherical colloids of similar size (*11*, *12*, *15*).

Square-shaped platelets aggregate at angles intermediate between 0 and 90° relative to $\mathbf{n_0}$, suggesting a nondipolar symmetry of elastic interactions. A time series of video frames in Fig. 3A shows two interacting squares after release from the optical traps used to position them initially with **R** parallel to $\mathbf{n_0}$. The squares repel while gradually moving sideways (frames 1 and 2), then attract along ≈45° to $\mathbf{n_0}$ (frames 3 and 4), and ultimately aggregate with adjacent sides touching to form a chain that equilibrates at ≈40° to $\mathbf{n_0}$. This equilibration angle decreases with the addition of more particles into the linear chain, consistent with the planar anchoring at the NLC-colloid surfaces. Kinked chains as well as more symmetric structures are also possible. For example, a square and a two-particle chain can attract (Fig. 3, C and D) and form a structure in which the individual square orientations match those of isolated ones.

To elucidate the angular dependence of elastic interactions between square particles, two are positioned at a fixed center-to-center separation of $R = 12.3$ μm and various angles between **R** and $\mathbf{n_0}$: $\theta = 0, \pm\pi/8, \pm\pi/4$, and $3\pi/8$, as shown in the inset of Fig. 3E. For each θ, the particles are released from the optical traps, tracked with video microscopy for 13 s while the traps are off, and then moved back to the same initial locations. Because the elastic forces at $R = 12.3$ μm are weak ($\sim 10^{-2}$ pN), we time-average an ensemble of 10 particle trajectories for each θ to mitigate the effects of Brownian motion. The average relative trajectories at various θ are shown in Fig. 3E. Elastic repulsion occurs for pair orientations parallel ($\theta = 0$) and perpendicular ($\theta = \pi/2$) to $\mathbf{n_0}$, whereas strong attraction along **R** takes place at $\theta = \pm\pi/4$. At $\theta = \pm\pi/8$, the elastic force drives the particles sideways toward $\theta = \pm\pi/4$ while gradually becoming attractive. The angular dependence of the expected force between quadrupoles at a large fixed separation

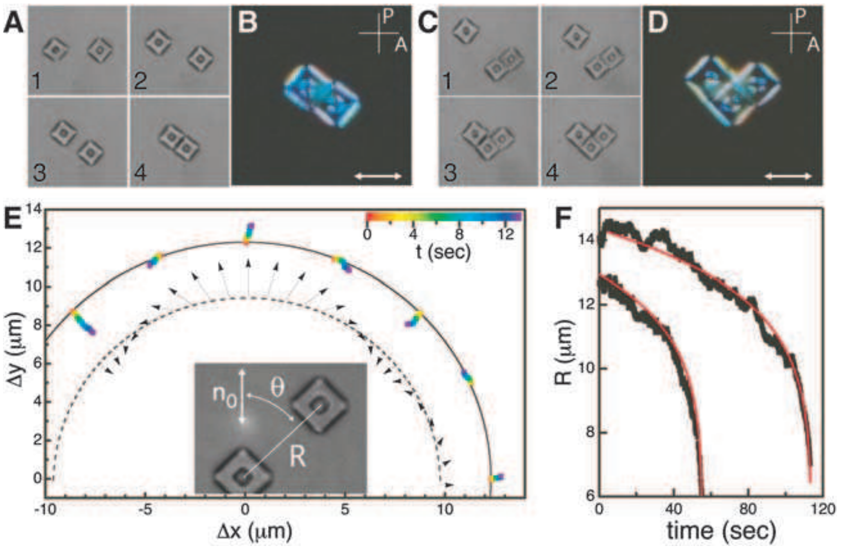

Fig. 3. Quadrupolar elastic interactions of square platelets and their assembly in 5CB. (**A**) Video frames (1 to 4) showing squares released from optical traps with their initial center-to-center separation **R** parallel to $\mathbf{n_0}$ (horizontal). Elastic interactions drive the particles to form a chain at ≈40° to $\mathbf{n_0}$. The elapsed times for each frame are: (1) 0 s, (2) 60.2 s, (3) 77.7 s, and (4) 81.3 s. (**B**) PM image of the two-square chain formed in (A). (**C**) Video frames (1 to 4) showing the aggregation of a square with a two-square chain resulting in a structure symmetric about the plane orthogonal to $\mathbf{n_0}$. The elapsed times in each frame are: (1) 0 s, (2) 40.5 s, (3) 53.3 s, and (4) 56.2 s. (**D**) PM micrograph of the aggregate formed in (C). (**E**) Relative displacements Δx, Δy of square platelets that are color-coded as a function of elapsed time (inset) after being released with the initial separation $R = 12.3$ μm. The data sets are obtained by particle tracking and provided for the initial pair-separation vector **R** at angles $\theta = 0, \pm\pi/8, \pm\pi/4$, and $3\pi/8$ relative to $\mathbf{n_0}$. Black arrows indicate the quadrupolar pair interaction force at large fixed separation R and various θ. (**F**) $R(t)$ dependences for a pair of squares with initial separations $R_0 = 14.3$ μm and 12.9 μm. Red lines show least-squares fits with the $R(t)$ expected for a quadrupolar interaction balanced by a viscous drag. The orientation of the far-field director $\mathbf{n_0}$ is shown by the white double-headed arrows in (B) and (D).

(shown by black arrows in Fig. 3E) (*9*, *15*) exhibits marked correlation with the measured displacements, confirming the quadrupolar nature of elastic forces between colloidal squares. These results imply that the presence of the hole in a colloidal square and, more generally, other modifications to the platelet's topology are inconsequential to the anisotropy of interactions, as long as the quadrupolar $\mathbf{n}(\mathbf{r})$ symmetry is preserved.

Quadrupolar forces are expected to decay with distance as ~R^{-6} (*9*, *15*). To test if square platelets interact in this manner, we have measured the relative positions of two colloidal squares along $\theta = \pi/4$ from initial separations R_0 = 14.3 and 12.9 μm (Fig. 3F). From a balance of a quadrupolar elastic force $F_{\mathrm{elq}} = -\kappa_q/R^6$ with a viscous drag, one obtains the time-dependent particle separation $R(t) = (R_0^7 - 7\alpha_q t)^{1/7}$, where $\alpha_q = \kappa_q/\zeta$. The two sets of data in Fig. 3F can be fit with $R(t)$ using only one adjustable parameter $\alpha_q = (1.6 \pm 0.1) \times 10^5\ \mu\mathrm{m}^7/\mathrm{s}$. Taking the average elastic constant $K \approx 7$ pN (*30*), an effective viscosity $\eta \approx 0.075$ Pa·s for 5CB, as well as the side length L = 4.5 μm of the platelet, dimensional analysis gives an estimate of $\alpha_q \sim KL^5/\eta = 1.7 \times 10^5\ \mu\mathrm{m}^7/\mathrm{s}$, in reasonable agreement with these experiments. Using a drag coefficient $\zeta \approx 1.9 \times 10^{-6}$ kg/s of a square platelet in 5CB [determined by probing its diffusive motion with video microscopy (fig. S3)] and $\alpha_q = 1.6 \times 10^5\ \mu\mathrm{m}^7/\mathrm{s}$, we calculate a maximum attractive elastic force of ≈20 pN near contact at R = 4.5 μm and corresponding binding energy ≈3 × 10^{-17} J (≈7000k_BT).

In conclusion, elastic colloidal interactions in NLCs are sensitive to the colloids' shapes. Equilibrium director field configurations around equilateral polygonal colloids exhibit dipolar symmetry if they have odd N (i.e., triangles or pentagons) and quadrupolar symmetry if N is even, giving rise to dipolar and quadrupolar elastic colloidal interactions, respectively. Elastic dipole moments of polygonal platelets orient perpendicular to the far-field director $\mathbf{n_0}$. Dipole-dipole forces drive their assembly into chains perpendicular to $\mathbf{n_0}$ if their dipoles are parallel and chains along $\mathbf{n_0}$ if their dipoles are antiparallel. Although the symmetry of these highly directional elastic forces should not change over a broad range of particle sizes (~50 nm to tens of microns), the strength can vary substantially. One can envision the design of such interactions for the assembly of colloidal architectures ranging from anisotropic aggregates to new types of colloidal crystals and optical metamaterials with well-defined alignment relative to the far-field director.

References and Notes

1. G. M. Whitesides, B. Grzybowski, *Science* **295**, 2418 (2002).
2. V. J. Anderson, H. N. Lekkerkerker, *Nature* **416**, 811 (2002).
3. K. Zhao, T. G. Mason, *Phys. Rev. Lett.* **99**, 268301 (2007).
4. K. J. Stebe, E. Lewandowski, M. Ghosh, *Science* **325**, 159 (2009).
5. T. C. Halsey, *Science* **258**, 761 (1992).
6. S. C. Glotzer, *Science* **306**, 419 (2004).
7. P. Poulin, H. Stark, T. C. Lubensky, D. A. Weitz, *Science* **275**, 1770 (1997).
8. P. M. Chaikin, T. C. Lubensky, *Principles of Condensed Matter Physics* (Cambridge Univ. Press, Cambridge, 2000).
9. H. Stark, *Phys. Rep.* **351**, 387 (2001).
10. I. I. Smalyukh, A. V. Kachynski, A. N. Kuzmin, P. N. Prasad, *Proc. Natl. Acad. Sci. U.S.A.* **103**, 18048 (2006).
11. I. Musevic, M. Skarabot, U. Tkalec, M. Ravnik, S. Zumer, *Science* **313**, 954 (2006).
12. M. Vilfan *et al.*, *Phys. Rev. Lett.* **101**, 237801 (2008).
13. I. Dierking, G. Biddulph, K. Matthews, *Phys. Rev. E* **73**, 011702 (2006).
14. J.-C. Loudet, P. Barois, P. Poulin, *Nature* **407**, 611 (2000).
15. I. I. Smalyukh, O. D. Lavrentovich, A. N. Kuzmin, A. V. Kachynski, P. N. Prasad, *Phys. Rev. Lett.* **95**, 157801 (2005).
16. A. B. Nych *et al.*, *Phys. Rev. Lett.* **98**, 057801 (2007).
17. J. C. Crocker, D. G. Grier, *J. Colloid Interface Sci.* **179**, 298 (1996).
18. C. J. Hernandez, T. G. Mason, *J. Phys. Chem. C* **111**, 4474 (2007).
19. Materials and methods are available as supporting material on *Science* Online.
20. D. G. Grier, *Nature* **424**, 810 (2003).
21. I. I. Smalyukh, S. V. Shiyanovskii, O. D. Lavrentovich, *Chem. Phys. Lett.* **336**, 88 (2001).
22. C. Tsakonas, A. J. Davidson, C. V. Brown, N. J. Mottram, *Appl. Phys. Lett.* **90**, 111913 (2007).
23. C. Lapointe *et al.*, *Science* **303**, 652 (2004).
24. U. Tkalec, M. Skarabot, I. Musevic, *Soft Matter* **4**, 2402 (2008).
25. F. Brochard, P. G. de Gennes, *J. Phys. (Paris)* **31**, 691 (1970).
26. T. C. Lubensky, D. Pettey, N. Currier, H. Stark, *Phys. Rev. E* **57**, 610 (1998).
27. B. I. Lev, S. B. Chernyshuk, P. M. Tomchuk, H. Yokoyama, *Phys. Rev. E* **65**, 021709 (2002).
28. Because of a density mismatch of ~0.2 g/cm^3 between SU-8 and 5CB, particles tend to sediment toward the lower half of the cell and come to rest at a height ≈5 μm at which the repulsive particle-substrate interaction due to the $\mathbf{n}(\mathbf{r})$ deformations balances gravity (*23*).
29. The drag coefficient of a triangular platelet can be estimated as that of a thin disk with the radius a circumscribing the edges of the triangle: $\zeta \approx 32\eta a/3$. Using a representative value of shear viscosity $\eta \approx 0.075$ Pa•s for 5CB (*9*), one finds $\zeta \approx 2 \times 10^{-6}$ kg/s. Although this analysis is only approximate, it gives reasonable estimates for platelet colloids, as verified experimentally (*19*).
30. L. M. Blinov, V. G. Chigrinov, *Electrooptic Effects in Liquid Crystal Materials* (Springer, New York, 1996).
31. We thank K. Zhao for assistance with the fabrication of colloids, and we acknowledge support from the Institute for Complex and Adaptive Matter and from NSF grants DMR 0645461, DMR 0847782, CHE 0450022, and DMR 0820579.

Supporting Online Material
www.sciencemag.org/cgi/content/full/326/5956/1083/DC1
Materials and Methods
Figs. S1 to S3
References

20 May 2009; accepted 15 September 2009
10.1126/science.1176587

Atmospheric Sulfur in Archean Komatiite-Hosted Nickel Deposits

Andrey Bekker,[1, 2*†] Mark E. Barley,[3*] Marco L. Fiorentini,[3] Olivier J. Rouxel,[4] Douglas Rumble,[1] Stephen W. Beresford[3]

Some of Earth's largest iron-nickel (Fe-Ni) sulfide ore deposits formed during the Archean and early Proterozoic. Establishing the origin of the metals and sulfur in these deposits is critical for understanding their genesis. Here, we present multiple sulfur isotope data implying that the sulfur in Archean komatiite-hosted Fe-Ni sulfide deposits was previously processed through the atmosphere and then accumulated on the ocean floor. High-temperature, mantle-derived komatiite magmas were then able to incorporate the sulfur from seafloor hydrothermal sulfide accumulations and sulfidic shales to form Neoarchean komatiite-hosted Fe-Ni sulfide deposits at a time when the oceans were sulfur-poor.

Submarine Fe-Ni sulfide deposits hosted in komatiites (mantle-derived ultramafic rocks with high magnesium content) produce ~10% of the world's annual Ni, making them an important type of ore-bearing deposits (*1*). Mineralization of komatiite-hosted Fe-Ni sulfides can form either massive ores at the base of, or disseminated/blebby ores within, komatiite lava flows and sills (fig. S1). Komatiite-hosted massive Fe-Ni sulfide deposits are most abundant during periods of elevated mantle plume magmatism and continental crustal growth. In the Neoarchean and Paleoproterozoic, such events occurred around 2.95, 2.7, and 1.9 billion years ago (Ga), which correspond to global peaks in the abundance of banded iron formations, sulfidic black shales, and volcanogenic massive Fe-Cu-Zn sulfide deposits (*2*, *3*).

Initial efforts to determine the source of sulfur in these deposits suggested that sulfides were transported directly from the mantle (*4*, *5*). It was later proposed based on a wide range of volcanological, stratigraphic, geochemical, sulfur isotopic, thermodynamic, and fluid dynamic constraints that the magmas assimilated sulfur either during ascent or emplacement on the sea floor [see (*1*) for case studies] because the sulfur content of the mantle is too low (*6*), komatiites result from high degrees of melting in the mantle, and a negative pressure feedback on sulfur content limits sulfide saturation in mafic magmas (*7*). Analysis of multiple sulfur isotopes makes it

Supporting Online Material

Shape Controlled Colloidal Interactions in Nematic Liquid Crystals

Clayton P. Lapointe[1,2], Thomas G. Mason[2], and Ivan I. Smalyukh[1,1]

[1]*Department of Physics and Liquid Crystals Materials Research Center, University of Colorado at Boulder, Boulder, CO 80309, USA*

[2]*Department of Chemistry and Biochemistry, Department of Physics and Astronomy, and California NanoSystems Institute, University of California - Los Angeles, Los Angeles, CA 90095, USA*

I. Materials and Methods

1. Sample Preparation

Using photolithography, we fabricated colloids shaped as regular polygonal platelets with the uv-sensitive epoxy photoresist SU-8 2001 (Microchem) (*S1*). First, a sacrificial layer consisting of SU-8 without photo-initiator dissolved in cyclopentanone (concentration ≈29 %wt) was spin coated onto a 5-inch Si wafer and pre-baked on a hot plate yielding a thickness 1 μm. Next, the second 1 μm thick layer of photosensitive SU-8 2001 was spin coated on top of the sacrificial layer and pre-baked. The wafers were exposed to 365 nm light in an Ultratech 2145 i-line reduction stepper (5x reduction, 0.35 μm feature size) using a reticle-photomask (Toppan). After exposure, the wafers were developed in an organic solvent, SU-8 developer (1-methoxy-2-propyl acetate), which dissolves the underlying sacrifical layer as well as the uncrosslinked resist in the top layer releasing crosslinked SU-8 particles into the developer. Excess SU-8 polymer dissolved in the particle-SU-8 developer suspension was removed by repeated centrifugation and washing with fresh SU-8 developer. Particles were then transferred into the room temperature NLC 5CB (Frinton Labs) by solvent exchange. A small volume (≈100 μL) of the particles in SU-8 developer suspension was mixed thoroughly with 1 mL of 5CB and placed in the chamber of a

---

[1] Email: ivan.smalyukh@colorado.edu

vacuum convection oven held at an elevated temperature of 60 C. The samples were left in the oven under vacuum for 24 hours to completely evaporate the SU-8 developer out of the solution. The presence of residual dissolved SU-8 developer in the particle-5CB dispersion was monitored by determining the nematic-isotropic transition temperature T_{NI} of the samples using polarizing microscopy equipped with a heating stage (Instec). In all prepared samples, T_{NI} did not deviate more than 1 C from the T_{NI} = 35 C of pure 5CB. To adequately disperse the particles before filling the sample cells, the suspensions were agitated vigorously in an ultra-sonic bath at a temperature above T_{NI} for 2 hours. For the FCPM studies, 5CB was doped with the fluorescent dye n,n'-bis(2,5-di-tert-butylphenyl)-3,4,9,10-perylenedicarb-oximide (BTBP) at concentration of 0.01 wt. %, which is sufficient to produce a strong fluorescence signal for the director reconstruction without altering the NLC properties. The studied 10-60 μm cells consisted of glass plates with inner surfaces having spin coated thin films of baked and rubbed polyimide PI-2555 (HD Microsystems). Unidirectional rubbing of the coatings allowed for uniform alignment of 5CB defining the far-field director $\mathbf{n_0}$.

2. Video Microscopy, Optical Manipulation, and Fluorescence Confocal Imaging

Optical tweezers are widely used to manipulate colloidal particles (*S2*), including anisotropic colloids suspended in isotropic fluids (*S3*). We have utilized a holographic optical tweezers (HOT) setup that enables the alignment of platelet colloids with their long-axes parallel to either the focal lateral or axial planes (*S3*) of the microscope. In our HOT apparatus, a collimated beam from a ytterbium-doped fiber laser (IPG Photonics, λ = 1064 nm) is reflected off of a liquid crystal spatial light modulator (Boulder Nonlinear Systems) and coupled into the back aperture of a high numerical aperture 100x objective with a dichroic mirror. A rotatable half-wave plate is used to control the beam's polarization state. Computer generated holograms are calculated in real time and relayed to the spatial light modulator using the software package HOTgui (Arryx Inc.). The colloids used in our experiments consist of crosslinked SU-8 with refractive index $n_p \approx 1.6$ intermediate between the extraordinary and ordinary refractive indices of 5CB for light polarized parallel to, $n_e = n_{||} \approx 1.7$, and perpendicular to, $n_o = n_{\perp} \approx 1.5$, the nematic director, respectively. To facilitate stable optical trapping of SU-8 colloids in 5CB, we polarize the input beam of our optical tweezer setup perpendicular to $\mathbf{n_0}$, so that the effective refractive index of the surrounding nematic is lower than that of the particle. The linear polarization state of the optical traps is controlled with a rotatable half-wave plate. Furthermore, real-time control of the positions of optical traps allows for positioning particle pairs within the microscope's field of view as shown in Figs. 2 and 3. Images are acquired at a rate of 15 Hz with a charge-coupled device video camera (Flea 2, Point Grey Research) and stored on a personal computer for subsequent analysis.

We have used a FV300 Olympus confocal microscope in a FCPM mode (*S4*) to visualize the 3D structures of $\mathbf{n(r)}$. The excitation beam (488 nm Ar laser) is focused by an objective into a submicron volume in the BTBP-doped sample. Fluorescent light from this volume is detected by a photomultiplier tube in the spectral region 510-550 nm selected by interference filters. A pinhole positioned in a focal plane in front of the detector discriminates against the regions above and below the focal plane of the objective. The focused excitation beam scans the sample in horizontal planes at different fixed depths. Coordinate-dependent fluorescence intensity data are stored in the computer memory and then used to construct a 3-D image of the sample and compose its arbitrary cross-sections. An achromatic twisted-nematic linear polarization rotator is used to control the polarization of both excitation and detected fluorescent light; the director structures are reconstructed based on FCPM images obtained for different linear polarization states.

II. Director Field Configurations for Strong and Weak Surface Anchoring

The effect of reducing particle size and/or weakening the surface anchoring strength for spherical colloids with vertical surface anchoring is qualitatively different from the case of polygonal platelet colloids with planar anchoring as shown in Fig. S1. For spheres that promote strong vertical anchoring, the director field configuration is known to be dipolar with a hyperbolic hedgehog point defect outside the particle with dipole moment $\mathbf{p} \parallel \mathbf{n_0}$ (Fig. 1A); $\mathbf{n}(\mathbf{r})$ has one plane of broken mirror symmetry orthogonal to $\mathbf{n_0}$. However, both experimental (*S5*, *S6*) and theoretical (*S7*, *S8*) studies find this structure stable (minimizing energy) only for particle sizes larger than roughly 1 μm and strong surface anchoring. Reducing the radius a or weakening surface anchoring results in a transition to a configuration with a line defect that encircles the equator of the particle (Fig. S1B); the formed $\mathbf{n}(\mathbf{r})$ has no broken mirror symmetry planes and is therefore quadrupolar (*S10*-*S12*). Upon decreasing the size or surface anchoring further, the energetic cost due to relaxing the boundary conditions at the particle's surface becomes less than the energy cost of bulk defects and elastic distortions. Relaxing the vertical boundary conditions for $\mathbf{n}(\mathbf{r})$ at the sphere's surface results in transforming the bulk line defect into a surface line defect or into a configuration with no defects in the NLC (note that for certain director distortions one can still think of a "virtual" defect inside of the volume of the particle) and the bulk $\mathbf{n}(\mathbf{r})$ distortions decrease significantly (Fig. 1C). Furthermore, the elastic dipoles formed by colloid-defect pairs can transform into elastic quadrupoles upon application of external fields (*S13*, *S14*), confinement (*S15*-*S17*), etc. Note that during these transformations of defects and structures around colloidal spheres, the total topological charge (*S7, S12, S18*) is conserved and topological characteristics of defects in a nematic volume enclosed by a surface of given Euler characteristic satisfy the restrictions imposed by the Euler–Poincare and Gauss theorems, which is also true for non-spherical particles.

In contrast to the dipolar-quadrupolar symmetry changes exhibited by $\mathbf{n}(\mathbf{r})$ around spherical particles discussed above, the dipolar configuration formed by odd-N polygonal platelets with planar surface anchoring should be more stable with respect to varying particle size and strength of surface anchoring. The symmetry of **n**(**r**) does not change when either surface anchoring or size of an odd-*N* platelet such as a triangle is reduced (Figs. S1D and E); the deformations are smaller, and therefore, the magnitude of **p** is smaller than in the strong anchoring case, but the **n**(**r**) structure remains dipolar. This behavior is similar to the case of spherical colloids with planar surface anchoring retaining their quadrupolar symmetry of **n**(**r**) with varying the particle size and anchoring strength (Figs. S1J and K).

The above differences between the behavior of spherical and anisotropic colloids can be understood by considering the bulk elastic and surface anchoring energy associated with introducing the colloidal inclusions into the NLC. The Frank elastic energy of NLCs can be expressed in terms of spatial gradients of **n**(**r**):

$$U_{el} = \tfrac{1}{2}\int d^3\mathbf{r}\left[K_{11}\left(\nabla\cdot\mathbf{n}\right)^2 + K_{22}\left(\mathbf{n}\cdot\nabla\times\mathbf{n}\right)^2 + K_{33}\left(\mathbf{n}\times\nabla\times\mathbf{n}\right)^2\right] \qquad \text{(S1)}$$

where K_{11}, K_{22}, and K_{33} are three independent Frank elastic constants corresponding to "splay", "bend", and "twist" deformations respectively (*S18*) and the integration is carried out over the volume of the NLC. The three elastic constants of thermotropic small molecule nematics are of the same order of magnitude [e.g. for 5CB at room temperature $K_{11} \approx 6.4$ pN, $K_{22} \approx 3$ pN, and $K_{33} \approx 10$ pN (*S19*)]. In the one elastic constant approximation, Eq. (S1) is often approximated as

$$U_{el} = \tfrac{K}{2}\int d^3\mathbf{r}\left(\nabla\mathbf{n}\right)^2 \qquad \text{(S2),}$$

where K is the average of K_{11}, K_{22}, and K_{33}. Using the literature values for 5CB quoted above gives an average $K \approx 6.5$ pN.

For planar degenerate anchoring, the surface anchoring energy can be represented with the Rapini-Papoular expression (*S18*), which can be written as:

$$U_S = \tfrac{w}{2}\int_S d^2\mathbf{r}\left(\mathbf{n}\cdot\mathbf{b}\right)^2 \qquad \text{(S3),}$$

where w is the polar surface anchoring coefficent, **b** is a unit vector normal to the particle's surface (the preferred orientation of the molecules is parallel to the surface), and the integration is over the surface area of the platelet. For finite anchoring strength, the **n**(**r**) configuration that occurs for a given colloid is the one that minimizes the total energy including both the bulk Frank elastic and surface anchoring terms: $U_{tot}= U_{el} +U_S$; whereas in the strong anchoring limit ($w\rightarrow\infty$), one minimizes only U_{el} with fixed boundary conditions for **n**(**r**) on the surface of the colloid. Different than the case of a spherically symmetric particle, the total energy U_{tot} due to introducing a particle of complex shape into a NLC is minimized for certain well-defined orientations with respect to $\mathbf{n_0}$ allowing for the elastic alignment. Figure S2 demonstrates that this alignment is indeed due to nematic elasticity rather than caused by sample processing procedures.

Comparison of the Frank elastic energy in Eq. (S1) with the surface anchoring energy in Eq. (S3) gives a characteristic length $\xi=K/w$, often referred to as the surface extrapolation length (*S18*). The Frank energy due to introducing a particle of size a into a NLC with average elastic constant K scales as Ka whereas the surface energy scales as wa^2. In the limit $a>>\xi$, the anchoring is strong and the boundary conditions for **n**(**r**) on the surface of the colloid are rigid so that strong **n**(**r**) distortions and bulk/surface defects are needed to meet these boundary conditions. For $a<<\xi$, the surface anchoring is weak and the nematic can alleviate bulk deformations by relaxing the boundary conditions at the colloid's surface. This interplay between the surface anchoring and bulk elastic energies explains the symmetry changes for spherical particles discussed above. The situation is very different for odd-N platelet colloids that can introduce dipolar director distortions due to their shape even when the boundary conditions are relaxed. Scaling the platelet size down to ξ (Fig. 1E) at which minimization of surface anchoring energy given by Eq. (S3) is important, the symmetry of equilibrium director structure will still depend on shape of the particle. Therefore, the shape-dictated dipolar symmetry of **n**(**r**) should be retained even at particle sizes $a\sim\xi$, a regime at which the elastic dipoles formed by colloidal spheres and defects are not stable. Using $K\approx 6.5$ pN and an estimate of the polar surface anchoring coefficient $w\approx 10^{-4}$ J/m^2 for SU-8 and 5CB one obtains $\xi\approx 65$ nm. Assuming that the interaction energies are of order Ka, particles with sizes in the range a=50-100 nm (the size range of interest for potential applications such as self-assembly of optical metamaterials) are expected to bind with energy in the range (50-100)k_BT, suggesting that sub-micron nanoparticles could potentially be assembled via dipole-dipole interactions.

The symmetry of dipolar and quadrupolar elastic deformations around different polygonal colloids in the mid-plane of the platelet is similar to the far-field symmetry of $\mathbf{n}(\mathbf{r})$ arising from elastic dipoles and quadrupoles formed by $s=\pm½$ disclinations (strength s is defined as the number of revolutions by 2π that the $\mathbf{n}(\mathbf{r})$ makes when one circumnavigates the defect line once). For example, the dipolar $\mathbf{n}(\mathbf{r})$ far from the triangular platelet with $\mathbf{p}\perp\mathbf{n_0}$ (Fig. S1D and H) resembles the elastic deformations induced by a $s=\pm½$ disclination pair with $\mathbf{p}$ also orthogonal to $\mathbf{n_0}$ (Fig. S1F). This disclination dipole is known to be one of two low-energy dipolar defect geometries (*S20*) observed in small-molecule thermotropic NLCs (*S21*) as well as in polymer liquid crystals (*S22*). The quadrupolar $\mathbf{n}(\mathbf{r})$ induced by a square-shaped colloid (Figs. S1G and S1H) resembles the far-field director due to a quadropole of four $s=\pm½$ disclinations (Fig. S1I).

III. Viscous Drag of Polygonal Colloids in 5CB

Colloidal squares. Dissipative drag forces experienced by colloidal particles moving in NLCs are known to be quite complex due to the intricate coupling of orientational order to the flow fields induced by particle motion as well as the inherent anisotropy of shear viscosities of NLCs (*S24*). Nevertheless, in the Stokes regime, the drag force on a particle moving with velocity v in a uniformly aligned NLC can be expressed as $F_{\mathrm{drag}}= -\zeta_i\, v$ where ζ_i is a drag coefficient and the subscript i refers to motion either parallel to $\mathbf{n_0}$ ($i=\|$) or perpendicular to $\mathbf{n_0}$ ($i=\perp$). Using methods similar to those discussed in (*S24*, *S25*), we determined $\zeta_\|$ and $\zeta_\perp$ for a colloidal square in 5CB by measuring its anisotropic diffusive motion with video microscopy as shown in Fig. S3.

Particle displacements along and perpendicular to $\mathbf{n_0}$ (Δx and Δy, respectively) over various delay times τ were extracted from the trajectory data shown in Fig. S3A. Histograms sampled from the time-delayed displacements are well described by Gaussian distributions with different widths or mean-square displacements, $\sigma^2_{\parallel,\perp}$ (Fig. S3B). As is shown in Fig. S3C, the two mean-square displacements are linear in τ with different slopes corresponding to two different diffusivities, $D_{\parallel}$ and $D_{\perp}$. The slopes determined with least-squares fits (Fig. S3C) give diffusion constants $D_{\parallel}$ =(2.8±0.1)x10^{-3} μm^2/s and $D_{\perp}$=(1.9±0.1)x10^{-3} μm^2/s. The small offsets ≈5x10^{-3} μm^2 at τ=0 result from the noise floor of our image analysis algorithms. We use the Einstein relation, $D_i = k_BT/\zeta_i$ where k_B =1.38x10^{-23} J/K is Boltzmann's constant and T is temperature, to calculate the drag coefficients from the experimentally determined diffusion constants. Using T=298 K, we find $\zeta_{\parallel}$ = 1.5x10^{-6} kg/sec and $\zeta_{\perp}$ = 2.2x10^{-6} kg/sec. To estimate the elastic forces between square colloids in 5CB, we use the average drag coefficient $\zeta=(\zeta_{\parallel}+\zeta_{\perp})/2 \approx 1.9\text{x}10^{-6}$ kg/sec.

Colloidal triangles. We estimate the drag coefficient of a colloidal triangle in 5CB using an expression for the drag coefficient of a thin circular disk of radius a that circumscribes the triangular edges of our colloid (*S26*): $\zeta = 32\eta a/3 \approx 2\text{x}10^{-6}$ kg/sec where we used $\eta \approx 0.075$ Pa·s and a = 2 μm. This is a reasonable order of magnitude estimate, since estimating ζ for a square shaped colloid in the same fashion yields $\zeta \approx 4\text{x}10^{-6}$ kg/sec which is in a reasonable agreement with the value of 1.9x10^{-6} kg/s determined experimentally. Moreover, even for a spherical particle of the same radius a, one obtains a similar value of $\zeta = 6\pi\eta a \approx 6\text{x}10^{-6}$ kg/s. Although these estimates neglect the coupling of the nematic director to the flow field induced by the motion of the colloidal triangles, such simplified analysis is reasonable because the velocities of the particles are small (<1 μm/s) during the experiments.

SOM FIGURES

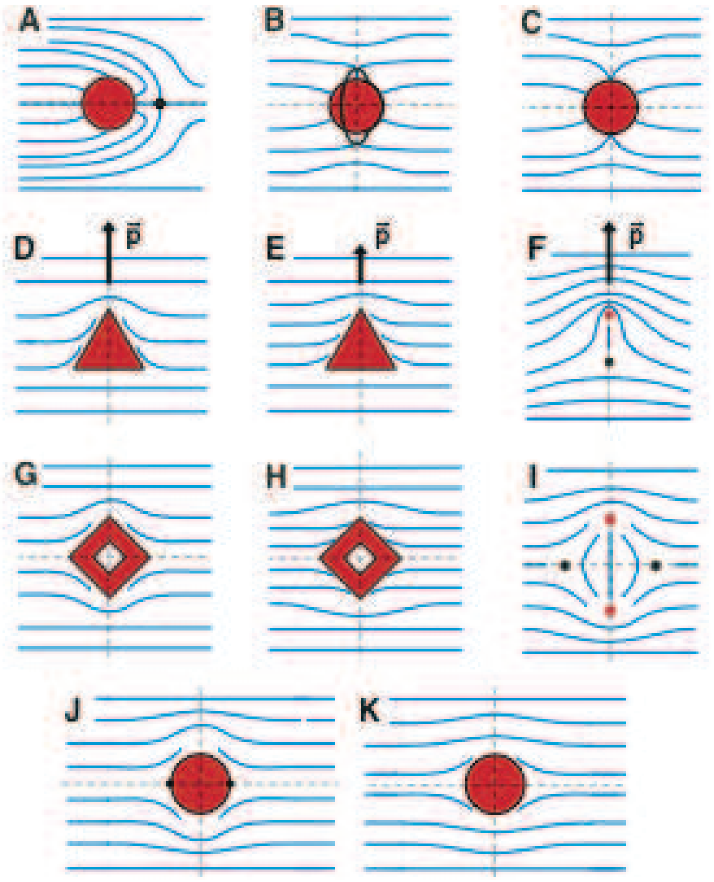

Fig. S1. Effects of surface anchoring and particle size on the symmetry of director structures induced by colloids. For spheres with vertical surface anchoring, reducing their size or weakening the surface anchoring changes the symmetry of **n**(**r**) from dipolar (**A**) to quadrupolar (**B**). The hedgehog point defect shown by black dot (A) transforms into the "Saturn ring" configuration with an equatorial s=-1/2 defect line shown by black line (B). (**C**) Further decrease of the particle size or surface anchoring strength results in the bulk defect line becoming a surface line defect or even a virtual defect with the director at the particle's surface deviating from the surface normal due to the relaxed boundary conditions, again giving quadropolar **n**(**r**). (**D**, **E**) In contrast, weakening the surface anchoring on a triangular colloid with planar anchoring does not change the **n**(**r**) symmetry from dipolar to quadrupolar. Although the distortions, and thus the magnitude of **p**, are smaller for weak surface anchoring, **n**(**r**) remains dipolar and resembles the far-field symmetry of distortions around a s=+1/2 (red dot) and s=-1/2 (black dot) dipolar pair of line defects with **p** oriented perpendicular to $\mathbf{n_0}$ (**F**). (**G**, **H**) Similarly, weakening the surface anchoring on a square colloid decreases the overall distortions, and thus the magnitude of the quadrupole moment is smaller; however, the quadrupolar symmetry of **n**(**r**) is retained and is similar to that of the far-field **n**(**r**) due to a quadrupole of s=+/-½ line defects (**I**). (**J**) For colloidal spheres with strong planar anchoring, **n**(**r**) is quadrupolar with two surface point defects (black dots) at the poles of the sphere along $\mathbf{n_0}$. (**K**) Decreasing anchoring and spherical particle size reduces the bulk deformations by relaxing the planar boundary condition for **n**(**r**) at the particle's surface yet there is no change in the quadrupolar symmetry of **n**(**r**).

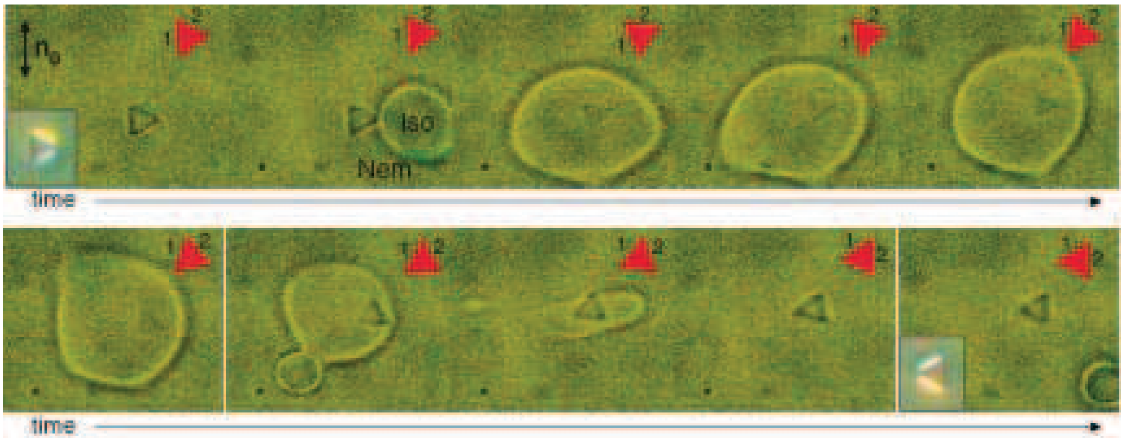

Fig. S2. Spontaneous alignment of triangular platelets with one side parallel to $\mathbf{n_0}$ due to nematic elasticity. Locally melting 5CB into the isotropic phase around a triangular colloid with a focused infrared laser beam demonstrates that the alignment of triangular particles relative to $\mathbf{n_0}$ is tri-stable and consistent with degenerate planar surface anchoring. Using an Instec heating stage, the sample is held at a temperature T=34 C near the nematic-isotropic transition temperature to facilitate local melting at relatively low laser powers (~0.3 W). A series of frames from a video show a triangular colloid rotated by 120° after locally heating the sample to form an isotropic bubble and then cooling back to the nematic phase. As shown in the top right of the first frame, the triangle is initially oriented such that side **1** is parallel to $\mathbf{n_0}$. In the next frame, a focused laser beam locally heats the 5CB sample to the right of the particle and nucleates an isotropic bubble which then expands around the colloid. Within the isotropic bubble the triangle rotates by 120° before the laser is turned off and the isotropic region quenches back to the nematic phase. After the quench, side **2** is now aligned along $\mathbf{n_0}$. Insets in the first and last frames show the particle under crossed polarizers. The elapsed time between frames is 0.13 s.

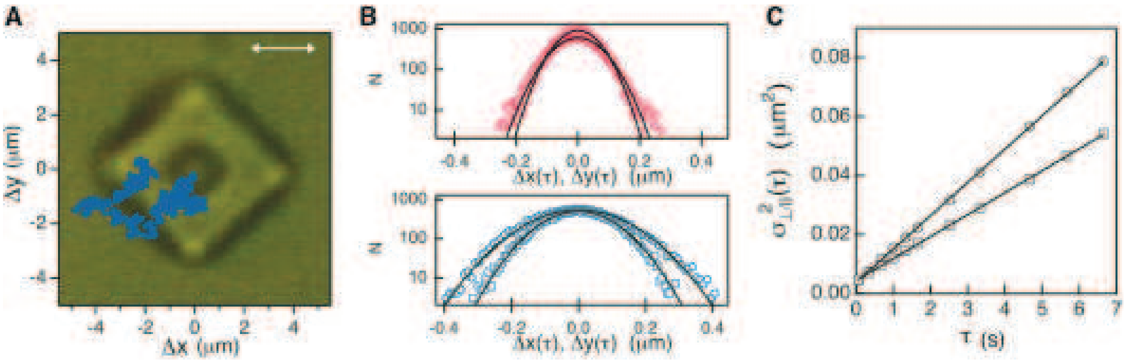

Fig. S3. Drag coefficients of a colloidal square in 5CB via diffusion measurements. (**A**) Blue points show the trajectory of the square in the background image determined from a video of total duration 1000 sec acquired at a frame rate of 15 Hz. The double-headed arrow shows the far-field alignment direction $\mathbf{n_0}$. (**B**) Histograms for displacements along the x-direction (circles) and the y-direction (squares) extracted from the trajectory data in (A) with sampling time delays of τ=0.33 sec (top) and τ=1.5 sec (bottom). Black lines show Gaussian fits to the histograms. (**C**) Mean square displacement $\sigma_{\parallel}^2$ parallel to $\mathbf{n_0}$ (circles) and $\sigma_{\perp}^2$ perpendicular to $\mathbf{n_0}$ (squares) as a function of τ. Slopes determined with linear fits to the data give values of the two diffusion constants corresponding to particle motion parallel to $\mathbf{n_0}$, $D_{\parallel}=(2.8\pm0.1)\text{x}10^{-3}$ μm^2/sec, and perpendicular to $\mathbf{n_0}$, $D_{\perp}=(1.9\pm0.1)\text{x}10^{-3}$ μm^2/sec.

SOM REFERENCES

(*S1*) C. J. Hernandez, T. G. Mason, *J. Phys. Chem. C* **111**, 4474 (2007).

(*S2*) A. Ashkin, *Proc. Natl. Acad. Sci.* **94**, 4853 (1997).

(*S3*) Z. Cheng, P. M. Chaikin, T. G. Mason, *Phys. Rev. Lett.* **89**, 108303 (2002).

(*S4*) I. I. Smalyukh, S. V. Shiyanovskii, O. D. Lavrentovich, *Chem. Phys. Lett.* **336**, 88 (2001).

(*S5*) O. Mondain-Monval, J. C. Dedieu, T. Gulik-Krzywicki, P. Poulin, *Eur. Phys. J. B* **12**, 167 (1999).

(*S6*) K. Kita, M. Ichikawa, Y. Kimura, *Phys. Rev. E* **77**, 041702 (2008).

(*S7*) H. Stark, *Eur. Phys. J. B* **10**, 311 (1999).

(S8) D. Andrienko, G. Germano, M. P. Allen, *Phys. Rev. E* **63**, 041701 (2001).

(*S9*) O. Guzmán, E. B. Kim, S. Grollau, N. L. Abbott, J. J. de Pablo, *Phys. Rev. Lett.* **91**, 235507 (2003).

(*S10*) P. Poulin, D. A. Weitz, *Phys. Rev. E* **57**, 626 (1998).

(*S11*) S. Zhang, E. M. Terentjev, A. M. Donald, *Macromol. Rapid Commun*. **26**, 911 (2005).

(*S12*) M. Kleman, O.D. Lavrentovich, *Philosophical Magazine* **86**, 4117 (2006).

(*S13*) J. C. Loudet, P. Poulin, *Phys. Rev. Lett.* **87**, 165503 (2001).

(*S14*) J. Fukuda, H. Yokoyama, *Eur. Phys. J. E* **21**, 341 (2006).

(*S15*) S. Grollau, N. L. Abbott, J. J. de Pablo, *Phys. Rev. E* **67**, 011702 (2003).

(*S16*) H. Stark, *Phys. Rev. E* **66**, 032702 (2002).

(*S17*) J. Fukuda, S. Zumer, *Phys. Rev. E* **79**, 041703 (2009).

(*S18*) P. G. de Gennes, J. Prost, *The Physics of Liquid Crystals* (Oxford Univ. Press, Oxford, 1993).

(*S19*) L. M. Blinov, V. G. Chigrinov, *Electrooptic effects in liquid crystal materials* (Springer-Verlag, New York, 1996).

(*S20*) F. Greco, L. Abbondanza, *Mol. Cryst. Liq. Cryst.* **188**, 155 (1990).

(*S21*) A. Bogi, P. Martinot-Lagarde, I. Dozov, M. Nobili, *Phys. Rev. Lett.* **89**, 225501 (2002).

(*S22*) B. A. Wood, E. L. Thomas, *Nature* **324**, 655 (1986).

(*S23*) H. Stark, D. Ventzki, *Phys. Rev. E* **64**, 031711 (2001).

(*S24*) J. C. Loudet, P. Hanusse, P. Poulin, *Science* **306**, 1525 (2004).

(*S25*) M. Skarabot, et al, *Phys. Rev. E* **73**, 021705 (2006).

(*S26*) W. Zhang, H. A. Stone, *J. Fluid Mech.* **367**, 329 (1998).